J. Fluid Mech. (2006), *vol.* 567, *pp.* 235–259. © 2006 Cambridge University Press
doi:10.1017/S0022112006002217 Printed in the United Kingdom

Passive dispersion in symmetrically interconnected layers under natural convection

By F. A. SANCHEZ[1,2] AND A. MEDINA[3,4]

[1]Departamento de Termoenergía, Facultad de Ingeniería, UNAM, 04510 Mexico City, Mexico
[2]División de Estudios de Posgrado, FIME-UANL, 66450 NL, Mexico
[3]Sección de Estudios de Posgrado e Investigación. ESIME-UPA-IPN, Mexico City, Mexico
[4]ETS Ingenieros Aeronáuticos, UPM, 28040 Madrid, Spain

(Received 2 February 2005 and in revised form 24 April 2006)

A numerical treatment of the natural convection and passive dispersion in symmetrically interconnected tilted layers embedded in a rock which is subject to a constant vertical temperature gradient is presented. Such a system is a faithful model of configurations commonly found in the geophysical context. There, flow movements and temperature distributions are closely connected to phenomena of interest such as transport of contaminants and diagenesis. The important case of large thermal conductivity of the rock compared with that of the material filling the layer is discussed in order to show the decisive role of the temperature distribution and the geometrical parameters on the convective flow. The present analysis treats two cases, the fluid-filled layer and the saturated porous layer. Convective flows were calculated for small Rayleigh numbers and the resulting velocity fields were included in the analysis of the transport of a passive contaminant that was initially located where layers connect with each other. Transport of contaminants in the isotropic porous layer was studied by using a model which includes hydrodynamic dispersion terms. How far the tracer transports through the layers and the rate the tracer enters into the system were analysed. The influence of the angle of tilt has also been included. The molecular diffusive Péclet number which relates convective to diffusive species transport is closely associated to a considerable transporting rate, and for the porous layer the hydrodynamic dispersion appears to be an important effect to consider.

1. Introduction

Fractured porous media are commonly involved in oil and water reservoirs, there, the interaction between fracture networks is of relevance. Underground fluid motion in these media may be caused by many different agents, including pressure gradients, capillary forces and buoyancy; the latter acts due on the temperature- or concentration-induced density differences. The fluid flow in these systems is relevant to the development of important phenomena such as the transport of minerals, radiative solutes or contaminants (Davis *et al.* 1985). Some consequences of such a transport may be the cementation and dissolution of minerals in rocks, the changes in some features of the layers and the eventual contaminant infiltration into water tables. Time scales for the transport of passive species, diagenesis and other phenomena in the geological field are strongly modified by the presence of convective flows even when they are weak. It is convenient to give a summary of the thermal convection in a single layer in order to contrast afterward the results found here.

https://doi.org/10.1017/S0022112006002217 Published online by Cambridge University Press

Fluid in the ground fills long tilted fractures embedded in rocks of geologic dimensions which are subject to temperature gradients of the order of the normal geothermal gradient estimated as 30–100 K km^{-1} (Wood & Hewett 1982). This condition may drive a low-Rayleigh-number natural convection in the fracture with fluid velocity currents of the order of 1 m per year. The heat transfer through the fracture does not increase owing to this convection; nevertheless, over geologic time scales, the mass flux accompanying this weak convection is able to transport heat and dissolved materials a significant distance along the fracture (Shaughnessy & Van Gilder 1995). In some systems such a process has been found to be enough to produce significant porosity changes (Hewett 1986), and also it has been shown that diffusive mass transfer is generally a negligible component of the total mass flux when characteristic distances are greater than grain diameters (Wood & Hewett 1982). The study of convective flow in single tilted layers includes two limit cases, the vertical and horizontal layers embedded in a solid affected by a vertical temperature gradient, which are commonly employed to model important geophysical phenomena. Vertical layers are used to model convection in saturated fractured rock zones such as those associated with faulting, while horizontal layers are considered for the analysis of convection and heat transfer in the Earth's upper mantle. For both cases, horizontal (Riahi 1983) and vertical (Wang, Kassoy & Weidman 1987) porous layers, the onset of convection is characterized by critical Rayleigh numbers which depend on the layer to solid thermal conductivity ratio. Additionally, the study of a single tilted layer embedded in a rock (Shaughnessy & Van Gilder 1995; Luna *et al.* 2002; Medina *et al.* 2002) yields valuable information about the nature of the thermal and superimposed phenomena such as the dispersive processes of passive contaminants (Luna *et al.* 2004). The oil industry is interested in the subterranean fluid flow because about 50 % of the oil originally located in typical fractured reservoirs cannot be collected by traditional (primary and secondary) recovery techniques, and this remaining oil is the main objective of modern enhanced oil recovery methods. Many natural porous systems are fractured and a deep understanding of them has become necessary. In addition to oil reservoirs, many groundwater resources and geothermal fields are also fractured. Thus, transport phenomena in fractured rocks have gained attention because of the growing concerns about enhanced oil production, pollution, water quality and geothermal power generation, among others. Additionally, in the last few decades, fractured media have been studied more because of their usefulness in designing insulation of radioactive waste, important heat and contaminant sources for underground water. Finally, there exist serious problems related to the current intense exploitation of groundwater and the increment of solute concentration in aquifers owing to leaking repositories and use of fertilizers.

The basic configuration of fractured media considers the generic case of a single straight fracture of infinite length embedded in an impermeable solid exposed to a background temperature gradient. The seminal works by Woods & Linz (1992) and Linz & Woods (1992) analysed convection and dispersion in infinite tilted fluid and saturated porous layers, respectively. Woods & Linz (1992) found accelerated transport of contaminants occurring in fluid-filled layers owing to the thermal convective effect on the diffusive one. They showed that the dispersion is capable of transporting a radioactive material, of half-life 10^4 years, tens of metres along a fracture within one half-life; without dispersion, the material would diffuse only a few metres along the fracture within the same time. Linz & Woods (1992) studied the transport of a passive tracer through a tilted saturated porous layer of infinite extent. Under geophysical conditions they found that dispersion not only enhances the ordinary diffusion of the

https://doi.org/10.1017/S0022112006002217 Published online by Cambridge University Press

tracers, but even dominates the spreading of passive particles in the flow. Furthermore, they described the variation of porosity with time as a function of the background-temperature gradient and the angle of tilt. The case of finite layers allows us to demonstrate the enormous influence of the layer and rock matrix thermal conductivities on the flow patterns. Natural convection has been studied in infinite (periodic) gently sine-like layers by Davis *et al.* (1985) and Hewett (1986), where indeed, the contrast between thermal conductivities has been taken into account. Studies on these layers were also extended to the porosity changes by dissolved matter in the fluid.

Symmetrically interconnected layers can be seen as a more complex case of a single folded layer. The system constituted by two interconnected straight layers is the simplest realization of fracture networks which yields results that are particularly interesting for understanding important geophysical phenomena. The present paper studies the problem of natural convection and passive dispersion in two interconnected tilted layers embedded in a rock. Despite its apparent simplicity, this study represents the first stage of work intended to give a better understanding of the transport phenomena in large networks affected by vertical temperature gradients. Two different kinds of interconnected tilted finite layers are analysed, the fluid-filled layers and the saturated porous layers. In both cases, the convective velocity fields were calculated for the small-Rayleigh-number regime and the influence of the angle of tilt was also included. In spite of the geometrical simplicity, our results show features of the convective flow that find application in passive dispersion phenomena in underground reservoirs. Indeed, the present work is intended to estimate the role thick fractures or layers play in transporting passive substances when the surrounding rock has a large thermal conductivity compared with that one of the material filling the layers. The resulting velocity fields were included in the analysis of the transport of a passive contaminant that enters the system through the layer walls, but only in a small region located where layers connect with each other. We are interested not only in determining how far the tracer transports through the layers, but also the rate at which the tracer enters the system. We include a discussion on the important differences between finite and infinite layers with respect to transport phenomena features.

2. Statement of the problem

The geometry analysed in this study consists of a two-dimensional horizontal slab of impermeable rock of finite width B and height H, where $H \ll B$. The rock contains two interconnected layers (or a folded layer) of width d and length h which cross the slab from base to base at an angle ϕ to the horizontal (figure 1*a*).

The rock thermal conductivity is k_s and the material which fills the layer has a thermal conductivity k_f. The upper and lower bases of the slab are kept at constant temperatures T_C and $T_H = T_C + \Delta T$, respectively. In the absence of the layers, a vertical thermal gradient $G = \Delta T/H$ would be present in the slab. Thus, far away from the layers it is expected that the isotherms will be horizontal, but near the layer they must be modified by the effect of the layer itself. Given the large variety of layers in an actual reservoir, the parameters $\Gamma = d/h$ and $\kappa = k_f/k_s$ are within a wide range of values, both large and small compared to unity (Phillips 1991). However, in the geophysical context, situations of enormous interest are those of a rock matrix containing fluid layers of water or oil, or porous layers saturated with either of those fluids. In such conditions, typical values are $\kappa \sim 0.1$, but combinations for which $\kappa \gg 1$ are also frequently found. Furthermore, typical values of porosity Φ in matrices are about 0.04 and in a typical porous layer Φ is about 0.45. Under those

https://doi.org/10.1017/S0022112006002217 Published online by Cambridge University Press

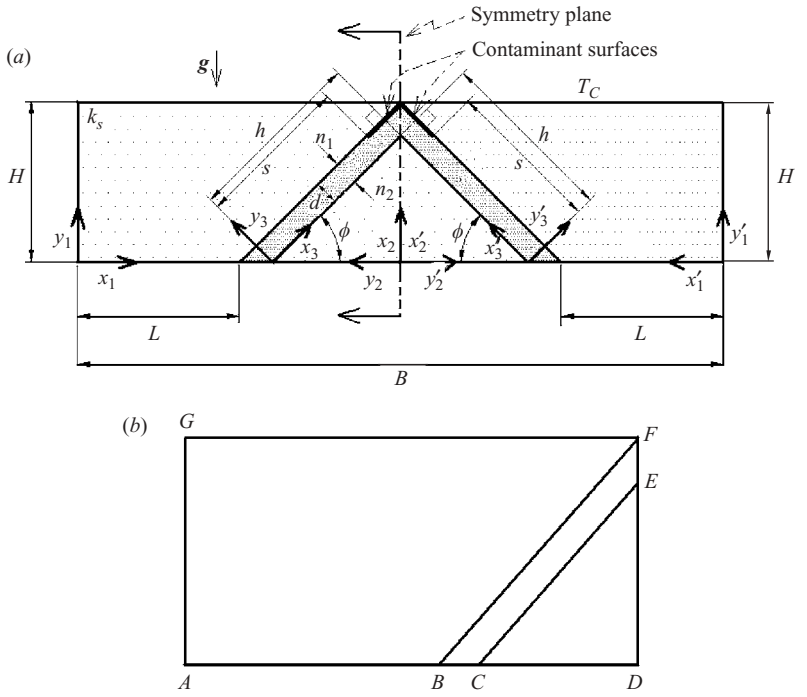


FIGURE 1. (*a*) Schematic of the physical model and coordinate systems. (*b*) Schematic of the region on the left-hand side.

conditions the matrix to layer permeability ratio is of order 10^{-4}. Thus, the matrix appears as almost impermeable with respect to its inner porous layer. Here, the rock matrix is considered as impermeable and cases corresponding to $\kappa/\Gamma \ll 1$ are studied in detail.

The present work can be seen as a local treatment of the general case of multiple parallel fractures, for instance, when multiple strata were simultaneously and permanently deformed. There pervious and impervious structures (with different rock properties such as thermal conductivity, permeability, fluid saturation) are present alternately, which yields structures like the one we studied here.

2.1. *Heat conduction in the rock*

As shown in figure 1(*a*), symmetry exists between the right-hand side coordinate systems $(1', 2', 3')$ and their corresponding systems at the opposite side $(1, 2, 3)$; thus for simplicity, we just analysed the last ones, the left-hand side, i.e. the region $ADFG$ in figure 1(*b*). The temperature distribution T_1 in the region $ABFG$ obeys the heat diffusion equation, $\nabla^2 T_1 = 0$, with the boundary conditions:

$$\left.\begin{array}{c} T_1 = T_C \quad \text{on} \quad FG, \quad T_1 = T_H \quad \text{on} \quad AB, \\ T_1 = T, \quad \partial T_1/\partial n_1 = \kappa \partial T/\partial n_1 \quad \text{on} \quad BF, \\ \partial T_1/\partial x_1 = 0 \quad \text{on} \quad AG, \end{array}\right\} \tag{2.1}$$

where T is the temperature within the layer. Moreover, in the triangular solid region CDE the heat diffusion equation, $\nabla^2 T_2 = 0$, is solved with the conditions:

$$\left.\begin{array}{c} T_2 = T_H \quad \text{on} \quad CD; \quad \partial T_2/\partial y_2 = 0 \quad \text{on} \quad DE, \\ T_2 = T, \quad \partial T_2/\partial n_2 = \kappa \partial T/\partial n_2 \quad \text{on} \quad CE. \end{array}\right\} \tag{2.2}$$

https://doi.org/10.1017/S0022112006002217 Published online by Cambridge University Press

2.2. *Convection in the fluid layer*

The steady-state flow in the fluid layer is modelled by continuity, momentum and energy equations, which are, respectively,

$$\nabla^* \cdot \boldsymbol{u}^* = 0, \tag{2.3}$$

$$(\boldsymbol{u}^* \cdot \nabla^*)\boldsymbol{u}^* = -\frac{1}{\rho}\nabla^* p + \nu \nabla^{*2}\boldsymbol{u}^* + \beta(T - T_C)\boldsymbol{g}, \tag{2.4}$$

$$(\boldsymbol{u}^* \cdot \nabla^*)T = \alpha_f \nabla^{*2} T, \tag{2.5}$$

where $\boldsymbol{u}^* = (u^*, v^*)$ is the two-dimensional velocity field and it is assumed that the fluid has kinematic viscosity ν, density ρ, thermal expansion coefficient β, and thermal diffusivity α_f; $\boldsymbol{g}$ is the gravity acceleration vector pointing downward, and $\nabla^* = \boldsymbol{i}\partial/\partial x^* + \boldsymbol{j}\partial/\partial y^*$. We considered constant fluid properties, steady-state flow, and the Boussinesq approximation had been applied. This set of equations was solved considering the impermeable and no-slip conditions on all the walls. Previous experimental studies showed that there is no mass exchange between the two tilted layers, at least for the small Rayleigh numbers here studied (Sánchez-Cruz 2005; Sánchez, Pérez-Rosales & Medina 2005). Therefore, in our numerical treatment, an impermeable imaginary wall on the symmetry plane (where layers connect each other) is assumed to exist. This last condition is valid only when the layers are symmetrically interconnected and both layers have the same length. If these requirements are not fulfilled, the resulting convection patterns in the layers are not similar each other and an interaction between the layers must exist. For the fluid layer, the temperature boundary conditions are $T = T_H$ at the lower wall BC, zero heat flux at the imaginary wall EF, and continuity for temperature and heat flux at the fluid to solid contact surfaces BF and CE.

2.3. *Convection in the saturated porous layer*

The flow in the fluid-saturated isotropic porous layer of permeability K is modelled by the continuity, energy and Darcy's equations. Constant fluid properties and steady-state flow are assumed, and the Boussinesq approximation is used. Consequently, as for the previous case, the continuity equation is stated by (2.3) where now $\boldsymbol{u}^* = (u^*, v^*)$ is the filtration velocity field, and the energy equation is given by (2.5), with α_f changed by α_m which is the effective thermal diffusivity of the porous medium. Darcy's equation is (Nield & Bejan 1999):

$$\boldsymbol{u}^* = -\frac{K}{\nu}\left(\frac{1}{\rho}\nabla^* p - \beta\,(T - T_C)\,\boldsymbol{g}\right). \tag{2.6}$$

The fluid which saturates the porous layer has kinematic viscosity ν, density ρ, thermal expansion coefficient β. All the walls are assumed to be impermeable. As above, it is considered that because of the symmetry there is no flow at the imaginary wall located on the symmetry plane in the joining zone. The temperature boundary conditions are the same as in the previous case.

2.4. *Transport of passive species in the layers*

The transport of contaminant species can be accelerated owing to the presence of macroscopic flows. Then, there exists a superposition of diffusive and convective flows. In general, variations in the species concentration cause changes in the fluid density and viscosity, which affect the flow regime that depends on those properties. However, at relatively low concentrations, the ideal tracer approximation is sufficient for most practical purposes (see Bear 1972). An ideal tracer consists of an inert substance with

https://doi.org/10.1017/S0022112006002217 Published online by Cambridge University Press

respect to its liquid and solid surroundings that does not affect the liquid properties. In order to estimate how the transport phenomenon of a passive contaminant takes place through the interconnected layers, the assumption of an ideal tracer is used for the fluid layer and the saturated porous layer.

As diffusion occurs under the effect of a macroscopic stream, the equation for the transport of the contaminant inside the fluid layer is:

$$\frac{\partial C^*}{\partial t^*} + (\boldsymbol{u}^* \cdot \nabla^*) C^* = D \nabla^{*2} C^*, \tag{2.7}$$

where C^* is the mass concentration, t^* is the time, and D is the diffusion coefficient of the species in the fluid. Then, as the velocity field is known, the dispersion is directly determined without any approximation.

The walls are impermeable except for a small region near the upper corner where it is assumed that the passive tracer is present as a contaminative surface with $C^* = C_{sat}$, where C_{sat} is the saturation concentration. The contaminative surfaces are located on the upper walls of the layers at $s \leqslant x_3^* \leqslant h + d\tan(\phi)$ (see figure 1a). In order to avoid difficulties in the numerical treatment arising from the real layer geometrical shape $BFEC$ of figure 1(b), the boundary condition on BC was simplified into a convenient form. A scale analysis shows that u_l, the local characteristic velocity in the fluid-filled layer, is given by $u_l \sim g\beta d^2 \Delta T_l \Gamma/\nu$, where ΔT_l is the local temperature difference across the layer. Then, $u_l/u_c \sim \Delta T_l/\Delta T$, where u_c is the characteristic velocity originated by a temperature difference across the layer of the order of ΔT. In our case, the convective motion near the lower edge (the wall BC) is negligible since $\Delta T_l/\Delta T \ll 1$ when $x_3^* \to 0$, as discussed in § 5.1. Thus, diffusion must drive the transport phenomena therein. Additionally, since BF and BC are impermeable walls, $\partial C^*/\partial y_3^* = 0$ on BF, and $\partial C^*/\partial n^* = \cos(\pi/2-\phi)\partial C^*/\partial x_3^* + \sin(\pi/2-\phi)\partial C^*/\partial y_3^* = 0$, where $\partial/\partial n^*$ denotes the derivative normal to the surface BC. The region limited by BC and $x_3^* = 0$ is of the order of $d^2/\tan\phi$, hence for slender layers with $\phi \neq 0$ such a region is very small compared with the whole layer and consequently $\partial C^*/\partial x_3^* \to 0$ at $x_3^* = 0$. Therefore, we considered the layer to begin at $x_3^* = 0$, and the region where $x_3^* < 0$ was neglected. After this truncation, the layer shape was modified, but no major effects on our solution were expected to appear since the contaminant source, the intense concentration gradients and significant convective velocity were distant from the $x_3^* = 0$ virtual wall. In this case the boundary conditions are:

$$\left.\begin{array}{c} \partial C^*/\partial x_3^* = 0 \quad \text{at} \quad x_3^* = 0, \quad \partial C^*/\partial y_3^* = 0 \quad \text{at} \quad y_3^* = 0, \\ \partial C^*/\partial y_3^* = 0 \quad \text{at} \quad y_3^* = d, \quad 0 < x_3^* < s, \\ C^* = C_{sat} \quad \text{at} \quad y_3^* = d, \quad s \leqslant x_3^* < h + d\tan(\phi), \\ \partial C^*/\partial n_3^* = 0 \quad \text{at} \quad x_3^* = h + y_3^* \tan(\phi), \quad 0 < y_3^* < d. \end{array}\right\} \tag{2.8}$$

where n_3^* denotes the derivative normal to the surface EF. In the second case, the saturated porous layer, the dispersion of the passive contaminant is more complex. As the mixing process is accelerated, improving the diffusion phenomenon within the small pores in the layer, the modelling equation results in (Bear 1972):

$$\Phi \frac{\partial C^*}{\partial t^*} + (\boldsymbol{u}^* \cdot \nabla^*) C^* = \Phi \nabla^* \cdot (\boldsymbol{D} \cdot \nabla^*) C^*, \tag{2.9}$$

where, C^* is the contaminant mass concentration, Φ is the porosity and $\boldsymbol{D}$ is the tensor of dispersion. A model for $\boldsymbol{D}$ corresponding to isotropic porous media presented by

https://doi.org/10.1017/S0022112006002217 Published online by Cambridge University Press

Bear (1972) yields:

$$\boldsymbol{D} = \begin{bmatrix} \dfrac{D}{\tau} + \dfrac{\alpha_l u^{*2} + \alpha_t v^{*2}}{\Phi\,|\boldsymbol{u}^*|} & \dfrac{(\alpha_l - \alpha_t)\, v^* u^*}{\Phi\,|\boldsymbol{u}^*|} \\ \dfrac{(\alpha_l - \alpha_t)\, u^* v^*}{\Phi\,|\boldsymbol{u}^*|} & \dfrac{D}{\tau} + \dfrac{\alpha_l v^{*2} + \alpha_t u^{*2}}{\Phi\,|\boldsymbol{u}^*|} \end{bmatrix}, \tag{2.10}$$

where α_l and α_t are the longitudinal and transversal dispersivities, respectively, and D is the binary molecular diffusion coefficient in the absence of the porous medium for the contaminant into the fluid, and τ is the tortuosity of the porous medium. From the continuity equation $v^* \sim \Gamma u^*$, and we assumed that $\alpha_l \approx \alpha_t \approx \alpha_D$, where α_D is the dispersivity coefficient. As $\Gamma \ll 1$, then $\boldsymbol{D}$ is simplified to:

$$\boldsymbol{D} = \left(\frac{D}{\tau} + \frac{\alpha_D |\boldsymbol{u}^*|}{\Phi}\right) \boldsymbol{I}, \tag{2.11}$$

where $\boldsymbol{I}$ is the identity tensor. Substituting (2.11) into (2.9):

$$\Phi \frac{\partial C^*}{\partial t^*} + u_3^* \frac{\partial C^*}{\partial x_3^*} + v_3^* \frac{\partial C^*}{\partial y_3^*} = \Phi \left(\frac{D}{\tau} + \frac{\alpha_D\,|\boldsymbol{u}^*|}{\Phi}\right) \left(\frac{\partial^2 C^*}{\partial x_3^{*2}} + \frac{\partial^2 C^*}{\partial y_3^{*2}}\right) + \alpha_D \left(\frac{\partial\,|\boldsymbol{u}^*|}{\partial x_3^*} \frac{\partial C^*}{\partial x_3^*} + \frac{\partial\,|\boldsymbol{u}^*|}{\partial y_3^*} \frac{\partial C^*}{\partial y_3^*}\right). \tag{2.12}$$

The boundary conditions are the impervious wall conditions, and again it is assumed that the contaminant enters the layers at the upper corner where the concentration is $C^* = C_{sat}$, the same as the problem of the fluid layer.

3. Dimensionless equations

A scale analysis shows that the suitable non-dimensional variables are:
For the solid regions:

$$\left.\begin{array}{l} x_1 = x_1^*/L, \quad y_1 = y_1^*/H, \quad \theta_1 = (T_1 - T_C)/\Delta T, \quad x_2 = x_2^*/H, \\ y_2 = y_2^* \tan(\phi)/H \quad (0 < \phi < \pi/2) \quad \theta_2 = (T_2 - T_C)/\Delta T, \\ \Delta T = T_H - T_C, \quad \kappa = k_f/k_s, \quad \Gamma_1 = H/L, \quad \Gamma_2 = 1/\tan(\phi). \end{array}\right\} \tag{3.1}$$

For the layer region:

$$\left.\begin{array}{l} x = x_3^*/h, \quad y = y_3^*/d, \quad u = u_3^*/u_c, \quad v = v_3^*/v_c, \\ \Gamma = d/h, \quad \theta = (T - T_C)/\Delta T, \end{array}\right\} \tag{3.2}$$

where u_c and v_c are the characteristic velocities, and α is the corresponding thermal diffusivity (α_f or α_m). In the fluid layer $u_c = \alpha_f Ra\Gamma/d$ and $v_c = \Gamma u_c$, where Ra is the Rayleigh number, $Ra = g\beta\Delta T d^3/(\alpha_f \nu)$. In the saturated porous layer, we find similarly the characteristic filtration velocities $u_c = \alpha_m Ra/d$ and $v_c = \Gamma u_c$ where $Ra = Kg\beta\Delta T d/(\alpha_m \nu)$.

So, the resulting dimensionless equations for the left solid regions are:

$$\Gamma_i^2 \frac{\partial^2 \theta_i}{\partial x_i^2} + \frac{\partial^2 \theta_i}{\partial y_i^2} = 0 \quad (i = 1, 2), \tag{3.3}$$

where 1 and 2 correspond to the external solid region and to the triangular solid region, respectively. Their corresponding boundary conditions couple the thermal problem in the rock with the thermal problem inside the cavity. The coupling,

https://doi.org/10.1017/S0022112006002217 Published online by Cambridge University Press

however, does not appear at leading order when $\kappa/\Gamma \ll 1$. Then the contact surfaces appear as approximately adiabatic and the boundary conditions become $\partial\theta_1/\partial n_1 = 0$ and $\partial\theta_2/\partial n_2 = 0$ at the contact surfaces, where $\partial/\partial n_1$ and $\partial/\partial n_2$ denote the derivatives normal to the contact surfaces (see figure 1*a*). Thus, temperature boundary conditions at the contact surfaces are simplified and the solid regions are solved independently from the fluid region.

If we introduce the streamfunction, $u = \partial\psi/\partial y, v = -\partial\psi/\partial x$, and the Prandtl number, $Pr = \nu/\alpha_f$, the dimensionless equations for the fluid layer corresponding to (2.4) and (2.5) are:

$$\left(\frac{\partial\psi}{\partial y}\right)\left[\frac{\partial^3\psi}{\partial x\partial y^2} + \Gamma^2\frac{\partial^3\psi}{\partial x^3}\right] - \left(\frac{\partial\psi}{\partial x}\right)\left[\Gamma^2\frac{\partial^3\psi}{\partial x^2\partial y} + \frac{\partial^3\psi}{\partial y^3}\right] = \frac{Pr}{Ra\Gamma^2}\frac{\partial^4\psi}{\partial y^4} + \frac{Pr\,\Gamma^2}{Ra}\frac{\partial^4\psi}{\partial x^4} + \frac{2Pr}{Ra}\frac{\partial^4\psi}{\partial y^2\partial x^2} + \frac{Pr\sin(\phi)}{Ra\Gamma^3}\frac{\partial\theta}{\partial y} - \frac{Pr\cos(\phi)}{Ra\Gamma^2}\frac{\partial\theta}{\partial x}, \quad (3.4)$$

$$\left(\frac{\partial\psi}{\partial y}\right)\frac{\partial\theta}{\partial x} - \left(\frac{\partial\psi}{\partial x}\right)\frac{\partial\theta}{\partial y} = \frac{1}{\Gamma^2 Ra}\left(\Gamma^2\frac{\partial^2\theta}{\partial x^2} + \frac{\partial^2\theta}{\partial y^2}\right). \quad (3.5)$$

After we introduced the stream function, the dimensionless equation for the motion in the saturated porous layer corresponding to (2.6) differentiated is:

$$\Gamma^2\frac{\partial^2\psi}{\partial x^2} + \frac{\partial^2\psi}{\partial y^2} = \sin(\phi)\frac{\partial\theta}{\partial y} - \Gamma\cos(\phi)\frac{\partial\theta}{\partial x}, \quad (3.6)$$

and the dimensionless energy equation corresponding to (2.5) is:

$$\left(\frac{\partial\psi}{\partial y}\right)\frac{\partial\theta}{\partial x} - \left(\frac{\partial\psi}{\partial x}\right)\frac{\partial\theta}{\partial y} = \frac{1}{\Gamma Ra}\left(\Gamma^2\frac{\partial^2\theta}{\partial x^2} + \frac{\partial^2\theta}{\partial y^2}\right). \quad (3.7)$$

There are two characteristic times, t_c, for the species transport process within the fluid layer, one time is related to the diffusive process, $t_c = d^2/D$, and the other is the convective time, $t_c = d/u_c$. Our analysis is focused on the effect of the convective motion, so we made time dimensionless with the diffusive time, hence $t = t^*D/d^2$. The concentration was made non-dimensional with the saturation concentration of the tracer in the fluid, $C = C^*/C_{sat}$. Therefore, the dimensionless tracer transport equation for the fluid layer corresponding to (2.7) is:

$$\frac{\partial C}{\partial t} + \Gamma Peu\frac{\partial C}{\partial x} + \Gamma Pev\frac{\partial C}{\partial y} = \Gamma^2\frac{\partial^2 C}{\partial x^2} + \frac{\partial^2 C}{\partial y^2}, \quad (3.8)$$

where $Pe = u_c d/D$ is the diffusive Péclet number, which is the ratio between the convective transport and the diffusive one. In the tracer transport process within the saturated porous layer, the diffusive characteristic time is $t_c = \tau d^2/D$ and the convective characteristic time is $t_c = d/u_c$, thus $t = t^*D/(\tau d^2)$. The dimensionless tracer dispersion equation for the saturated porous layer corresponding to (2.12) is:

$$\frac{\partial C}{\partial t} + \left(\frac{Pe\,\Gamma}{\Phi}u - \frac{Pe\,\Gamma^2}{\Phi Pe_\alpha}\frac{\partial|\boldsymbol{u}|}{\partial x}\right)\frac{\partial C}{\partial x} + \left(\frac{Pe\,\Gamma}{\Phi}v - \frac{Pe}{\Phi Pe_\alpha}\frac{\partial|\boldsymbol{u}|}{\partial y}\right)\frac{\partial C}{\partial y} = \left(1 + \frac{Pe}{Pe_\alpha}\frac{|\boldsymbol{u}|}{\Phi}\right)\left(\Gamma^2\frac{\partial^2 C}{\partial x^2} + \frac{\partial^2 C}{\partial y^2}\right), \quad (3.9)$$

where $Pe = \tau u_c d/D$ is the diffusive Péclet number and $Pe_\alpha = d/\alpha_D$ is the dispersive Péclet number.

https://doi.org/10.1017/S0022112006002217 Published online by Cambridge University Press

In both cases, fluid-filled layer and saturated porous layer, the dimensionless boundary conditions are:

$$\left.\begin{array}{l} \partial C/\partial x = 0 \quad \text{at} \quad x = 0, \quad \partial C/\partial y = 0 \quad \text{at} \quad y = 0, \\ \partial C/\partial y = 0 \quad \text{at} \quad y = 1, \quad 0 < x < s/h, \\ C = 1 \quad \text{at} \quad y = 1 \quad s/h \leqslant x \leqslant 1 + \varepsilon, \\ \partial C/\partial n_3 = 0 \quad \text{at} \quad x = 1 + \varepsilon y, \quad 0 < y < 1, \end{array}\right\} \tag{3.10}$$

where $\varepsilon = \Gamma \tan(\phi)$ and the initial concentration (at $t = 0$) within the layer is $C = 0$.

4. Numerical method

Since $\partial\theta_2/\partial n_2 = 0$ on EC, see figure 1, the solution in the region CDE is $\theta_2 = 1$. For solving the fluid-layer-region problem, (3.4) and (3.5) were linearized assuming that $(\partial\psi/\partial x)$ and $(\partial\psi/\partial y)$ were known from a previous iteration. So, $(\partial\psi/\partial x)$ and $(\partial\psi/\partial y)$ are substituted by $(\partial\psi^0/\partial x)$ and $(\partial\psi^0/\partial y)$, which are renewed after each iteration. In order to define a suitable mesh for our non-rectangular geometries, we introduced a simple non-orthogonal set of transformations. For the left-hand external solid region:

$$\left.\begin{array}{l} \xi_1 = x_1/(1 + \varepsilon_1\eta_1) \quad \text{where} \quad \varepsilon_1 = \Gamma_1 \tan(\pi/2 - \phi), \\ \qquad\qquad\qquad\quad \eta_1 = y_1, \end{array}\right\} \tag{4.1}$$

and for the fluid region:

$$\left.\begin{array}{l} \xi = x/(1 + \varepsilon\eta) \quad \text{where} \quad \varepsilon = \Gamma \tan(\phi), \\ \qquad\qquad\quad \eta = y. \end{array}\right\} \tag{4.2}$$

So, for the external solid region, the resulting diffusion equation from (3.3) for $i = 1$ is:

$$\frac{2\varepsilon_1^2\xi_1}{(1 + \varepsilon_1\eta_1)^2}\frac{\partial\theta_1}{\partial\xi_1} + \left(\left(\frac{\Gamma_1}{1 + \varepsilon_1\eta_1}\right)^2 + \left(\frac{\varepsilon_1\xi_1}{1 + \varepsilon_1\eta_1}\right)^2\right)\frac{\partial^2\theta_1}{\partial\xi_1^2} - \frac{2\varepsilon_1\xi_1}{1 + \varepsilon_1\eta_1}\frac{\partial^2\theta_1}{\partial\xi_1\partial\eta_1} + \frac{\partial^2\theta_1}{\partial\eta_1^2} = 0, \tag{4.3}$$

with the boundary conditions:

$$\left.\begin{array}{l} \partial\theta_1/\partial\xi_1 = 0 \quad \text{for} \quad \xi_1 = 0, \quad 0 \leqslant \eta_1 \leqslant 1, \\ \left(\dfrac{\Gamma_1\cos(-\pi/2 + \phi)}{1 + \varepsilon_1\eta_1} - \dfrac{\varepsilon_1\xi_1\sin(-\pi/2 + \phi)}{1 + \varepsilon_1\eta_1}\right)\dfrac{\partial\theta_1}{\partial\xi_1} \\ \quad + \sin(-\pi/2 + \phi)\partial\theta_1/\partial\eta_1 = 0 \quad \text{for} \quad \xi_1 = 1, \quad 0 \leqslant \eta_1 \leqslant 1, \\ \theta_1 = 1 \quad \text{for} \quad \eta_1 = 0, \quad 0 < \xi_1 < 1, \\ \theta_1 = 0 \quad \text{for} \quad \eta_1 = 1, \quad 0 < \xi_1 < 1. \end{array}\right\} \tag{4.4}$$

In the fluid layer, the equation of motion (3.4) at the non-orthogonal frame is:

$$A\frac{\partial^4\psi}{\partial\xi^4} + B\frac{\partial^4\psi}{\partial\xi^3\partial\eta} + C\frac{\partial^3\psi}{\partial\xi^3} + D\frac{\partial^2\psi}{\partial\xi^2} + E\frac{\partial^3\psi}{\partial\xi^2\partial\eta} + F\frac{\partial^4\psi}{\partial\xi^2\partial\eta^2} + G\frac{\partial\psi}{\partial\xi} + H\frac{\partial^2\psi}{\partial\xi\partial\eta} + I\frac{\partial^3\psi}{\partial\xi\partial\eta^2} + J\frac{\partial^4\psi}{\partial\xi\partial\eta^3} + K\frac{\partial^3\psi}{\partial\eta^3} + L\frac{\partial^4\psi}{\partial\eta^4} = M\frac{\partial\theta}{\partial\xi} + N\frac{\partial\theta}{\partial\eta}, \tag{4.5}$$

https://doi.org/10.1017/S0022112006002217 Published online by Cambridge University Press

where functions A to N are given in Appendix A, (A 1)–(A 14). The energy equation (3.5) is:

$$R\frac{\partial\theta}{\partial\xi}+S\frac{\partial^2\theta}{\partial\xi^2}+T\frac{\partial^2\theta}{\partial\xi\,\partial\eta}+U\frac{\partial^2\theta}{\partial\eta^2}+V\frac{\partial\theta}{\partial\eta}=0, \tag{4.6}$$

where functions R to V are given in the Appendix, (A 1)–(A 20). The boundary conditions at the non-orthogonal frame are:

$$\frac{\partial\psi}{\partial\eta}=\frac{\partial\psi}{\partial\xi}=\psi=0 \quad \text{for} \quad \begin{cases}\xi=0, & 0\leqslant\eta\leqslant1,\\ \xi=1, & 0\leqslant\eta\leqslant1,\\ \eta=0, & 0<\xi<1,\\ \eta=1, & 0<\xi<1,\end{cases} \tag{4.7}$$

$$\left.\begin{aligned}&\theta=1 \quad \text{for} \quad \xi=0, \quad 0\leqslant\eta\leqslant1,\\ &\left(\frac{\Gamma\cos(-\phi)}{1+\varepsilon\eta}-\frac{\varepsilon\xi\sin(-\phi)}{1+\varepsilon\eta}\right)\frac{\partial\theta}{\partial\xi}\\ &\quad+\sin(-\phi)\partial\theta/\partial\eta=0 \quad \text{for} \quad \xi=1, \quad 0\leqslant\eta\leqslant1,\\ &\theta=1 \quad \text{for} \quad \eta=0, \quad 0<\xi<1,\\ &\theta=\theta_1(\xi)|_{\xi_1=1} \quad \text{for} \quad \eta=1, \quad 0<\xi<1.\end{aligned}\right\} \tag{4.8}$$

In the saturated porous layer, the equation of motion (3.6) at the non-orthogonal frame is:

$$A\frac{\partial\psi}{\partial\xi}+B\frac{\partial^2\psi}{\partial\xi^2}+C\frac{\partial^2\psi}{\partial\xi\,\partial\eta}+D\frac{\partial^2\psi}{\partial\eta^2}=E\frac{\partial\theta}{\partial\xi}+F\frac{\partial\theta}{\partial\eta}, \tag{4.9}$$

where functions A to F are given in Appendix A, (A 21)–(A 26). The energy equation (3.7) is the same as stated by (4.6) where functions R to V for this case are given in the Appendix, (A 27)–(A 31). The boundary conditions for the saturated porous layer are (4.8) and:

$$\frac{\partial\psi}{\partial\eta}=0 \quad \text{for} \quad \begin{cases}\xi=0, & 0\leqslant\eta\leqslant1,\\ \xi=1, & 0\leqslant\eta\leqslant1,\end{cases} \tag{4.10}$$

$$\frac{\partial\psi}{\partial\xi}=0 \quad \text{for} \quad \begin{cases}\eta=0, & 0<\xi<1,\\ \eta=1, & 0<\xi<1.\end{cases} \tag{4.11}$$

In both the fluid-filled layer and the saturated porous layer, the species transport equation resulting from (3.8) or (3.9) is:

$$\frac{\partial C}{\partial t}+R\frac{\partial C}{\partial\xi}+S\frac{\partial^2C}{\partial\xi^2}+T\frac{\partial^2C}{\partial\xi\,\partial\eta}+U\frac{\partial^2C}{\partial\eta^2}+V\frac{\partial C}{\partial\eta}=0. \tag{4.12}$$

For the fluid-filled layer, functions R to V are given by (A 32) to (A 36) and for the saturated porous layer by (A 37) to (A 41). In both cases, the boundary conditions are:

$$\left.\begin{aligned}&\partial C/\partial\xi=0 \quad \text{for} \quad \xi=0, \quad 0\leqslant\eta\leqslant1,\\ &\left(\frac{\Gamma\cos(-\phi)}{1+\varepsilon\eta}-\frac{\varepsilon\xi\sin(-\phi)}{1+\varepsilon\eta}\right)\frac{\partial C}{\partial\xi}\\ &\quad+\sin(-\phi)\partial C/\partial\eta=0 \quad \text{for} \quad \xi=1, \quad 0\leqslant\eta\leqslant1,\\ &\partial C/\partial\eta=0 \quad \text{for} \quad \eta=0, \quad 0<\xi<1,\\ &\partial C/\partial\eta=0 \quad \text{for} \quad \eta=1, \quad 0<\xi<0.95,\\ &C=1 \quad \text{for} \quad \eta=1, \quad 0.95\leqslant\xi<1,\end{aligned}\right\} \tag{4.13}$$

https://doi.org/10.1017/S0022112006002217 Published online by Cambridge University Press

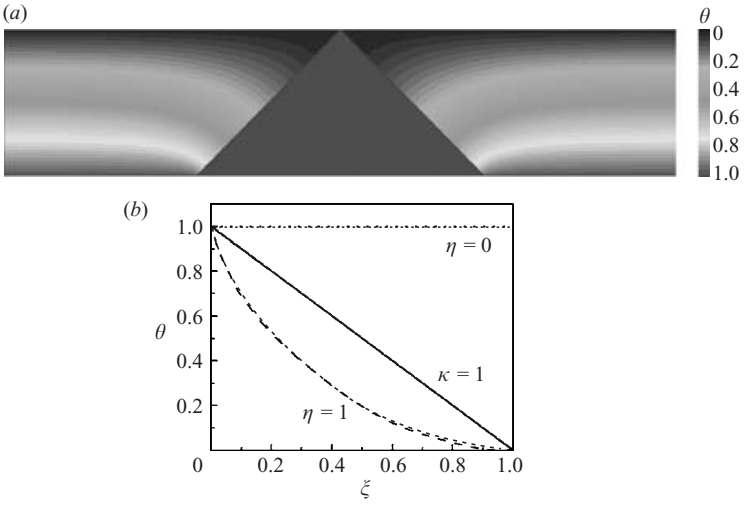


FIGURE 2. (*a*) Dimensionless temperature distribution in the rock. (*b*) Dimensionless temperature profiles along the lower ($\eta = 0$) and upper ($\eta = 1$) contact surfaces; the temperature distribution that would exist along the contact surfaces if κ were equal to unity is included.

where it has been considered that the contaminative surfaces extend from $\xi = 0.95$ to $\xi = 1$. After applying the variable transformations our non-rectangular geometries are transformed into squares, so, $0 \leqslant \xi \leqslant 1$ and $0 \leqslant \eta \leqslant 1$, which allowed us to use a simple mesh. Numerical solutions were obtained by using the conventional centred finite-difference method for the motion problem. For the species transport problem, diffusive terms used centred finite differences and convective terms used an UPWIND scheme when $Pe \geqslant 3$ and centred finite differences when $Pe < 3$. A mesh of 125×30 nodes was used, and a residual lower than 10^{-6} for each equation was the convergence criterion.

5. Results

5.1. *Temperature distribution in the rock*

A sample numerical solution for $\phi = \pi/4$ is shown in figure 2(*a*). Far away from the layer, the vertical temperature gradient is constant (horizontal isotherms), and as we approach the layer, the isotherms are strongly affected. Moreover, the existence of a single isotherm in the triangular solid region is evident. The reduced temperatures along the lower ($\eta = 0$) and upper ($\eta = 1$) contact surfaces are given in figure 2(*b*). These are the boundary conditions for the material in the layer. In order to observe how the presence of the layers affects the temperature distribution in the rock, figure 2(*b*) includes the temperature distribution that would exist along the contact surfaces if κ were equal to unity. In our particular case, where $\kappa \ll \Gamma$, the temperature differences between opposite points on the contact surfaces are of order ΔT and vary with ξ, and the critical change (equal to ΔT) takes place at the upper corner ($\xi = 1$). This peculiar situation is substantially different compared with what happens in the generic case of a single infinite tilted layer. In such a case, the temperature difference between opposite points on the contact surfaces remains constant along the slot (in both kinds of slots, fluid-filled or filled with a saturated porous medium) and it can be estimated from the angle of tilt, the Rayleigh number and the thermal

https://doi.org/10.1017/S0022112006002217 Published online by Cambridge University Press

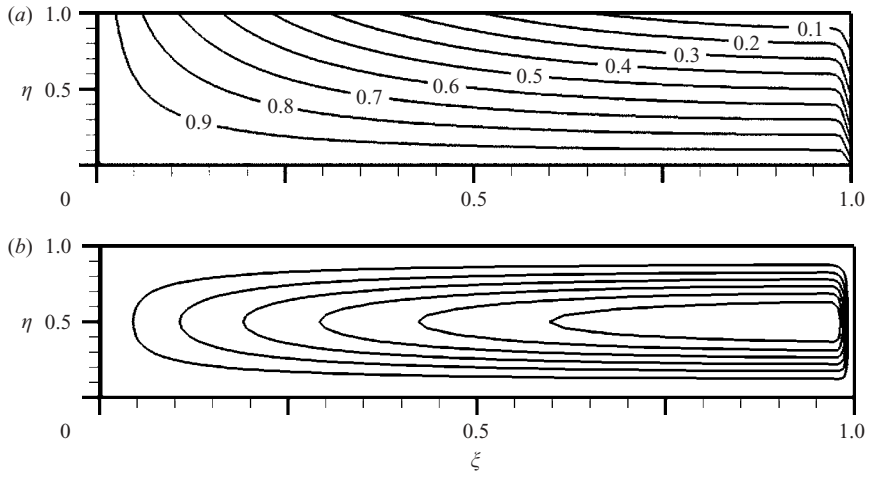


FIGURE 3. (*a*) Dimensionless temperature distribution within the fluid layer. (*b*) Streamlines within the fluid layer. In this case, $Ra = 1$, $Pr = 0.3645$, $\Gamma = 0.01$, $\phi = \pi/4$ and $\kappa \ll \Gamma$.

conductivity ratio (Linz & Woods 1992; Woods & Linz 1992). On the other hand, for finite fractures the temperature difference between opposite points on the contact surfaces varies along the slots (Luna *et al.* 2002) because of the end effects, and in the present case such a condition is specially notable. The heat flux across the finite layer, which has been neglected in the formulation of equations, is of order $k_f \Delta T/d$. This flux is small compared with the characteristic heat flux through the solid, $k_s \Delta T/H$, when $\kappa \ll \Gamma$, as was advanced before. If this condition is not satisfied, then the heat transfer problems in the solid and in the layer are coupled and should be solved simultaneously. The angle of tilt ϕ plays an important role in the thermal phenomenon. Far away from the layers, the vertical temperature gradient is constant (horizontal isotherms), and since the isotherms must be normal to the contact surfaces, as we approach the layer the isotherms are affected, strongly for small values of ϕ and weakly for large ones. Also, this is evident near the slot ends owing to the end effects are intensified when the angle of tilt becomes smaller.

5.2. *The fluid layer*

5.2.1. *The fluid flow*

Figure 3(*a*) presents the temperature distribution within the fluid layer in the non-orthogonal dimensionless coordinate system. The thermal diffusion is the main mean for the heat transfer in the layer, as a result of the weak convective flow, $Ra = 1$. The isotherms are only slightly affected by the flow. Indeed, since the Rayleigh numbers here analysed are small, $10^{-1} \leqslant Ra \leqslant 10$, the resulting weak convective flows do not affect the isotherms at all. So, figure 3(*a*) was found to be valid for that range of the Rayleigh number. The resulting flow is clearly two-dimensional as can be seen in figure 3(*b*), which shows the result for the stream function in the non-orthogonal coordinate system. Figure 3 corresponds to conditions commonly found in geothermal systems. The Prandtl number used for the numerical solution, $Pr = 0.3645$, corresponds to a typical value for heavy-oil at reservoir conditions, according to experimental measurements by Luna (2003), which makes this result particularly interesting. As could be expected from the temperature distribution in the rock, the flow arises longitudinally near the lower wall (where $\theta = 1$) throughout the layer and

https://doi.org/10.1017/S0022112006002217 Published online by Cambridge University Press

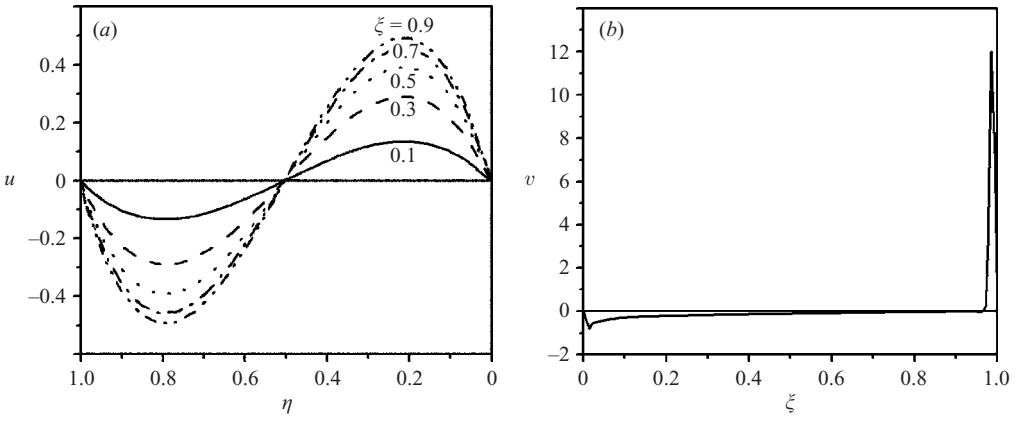


FIGURE 4. (*a*) Longitudinal velocity profiles at different locations within the fluid layer. (*b*) Transversal velocity profile at the middle plane, $\eta = 0.5$. In this case, $Ra = 1$, $Pr = 0.3645$, $\Gamma = 0.01$, $\phi = \pi/4$ and $\kappa \ll \Gamma$.

descends near the upper wall where the temperature is lower. Close to the upper corner, the flow suddenly changes its direction while at the lower region the change in direction is very slow and gentle. The longitudinal dimensionless velocity profiles within the layer are presented in figure 4(*a*). These profiles are symmetrical with respect to the middle plane $\eta = 0.5$, and as the fluid is warmed while it travels along the lower wall, the flow is faster at the upper region. The transversal velocity profile at the middle plane, $\eta = 0.5$ is shown in figure 4(*b*). This profile shows how fast the flow changes its direction at the upper corner and how slow this movement at the lower region is. Then, the convection motion within our finite slot allows us to observe the significant intensity of the transversal velocity, which is not considered in the analysis of infinite fractures since this component of the velocity appears because of the end effects. Therefore, the transport phenomena through the transversal direction in finite slots are due to diffusion and convection, whereas in the case of infinite slots there exists only diffusion through the transversal direction. The angle of tilt causes important effects on the shape of the convection cell. The strength of the convection motion in a single infinite slot embedded in solid slab is a maximum when $\phi = \pi/4$ (Luna *et al.* 2002), whereas for the present case, the intensity of convection augments when the angle of tilt increases, but it should be noted that in order to have two layers, ϕ cannot be equal to $\pi/2$.

Because the layer is under the conduction regime, it was found that the shape of the convective patterns and the dimensionless velocity are not affected by the Rayleigh number. Therefore, figures 3 and 4 are valid for $10^{-1} \leqslant Ra \leqslant 10$, when $Pr = 0.3645$, $\Gamma = 0.01$ and $\phi = \pi/4$. The effect of the Rayleigh number on the actual velocity is considered in the definition of the dimensionless velocity itself.

5.2.2. *Transient transport of a passive tracer*

As was mentioned before, the present analysis was intended to estimate the effect of the convective motion on the transport of a passive substance. In particular, our interest is focused on the transport of inert substances, such as nitrogen, through fluid layers and porous layers. As we know the convective motion, we are able to estimate the transport of the ideal tracer.

https://doi.org/10.1017/S0022112006002217 Published online by Cambridge University Press

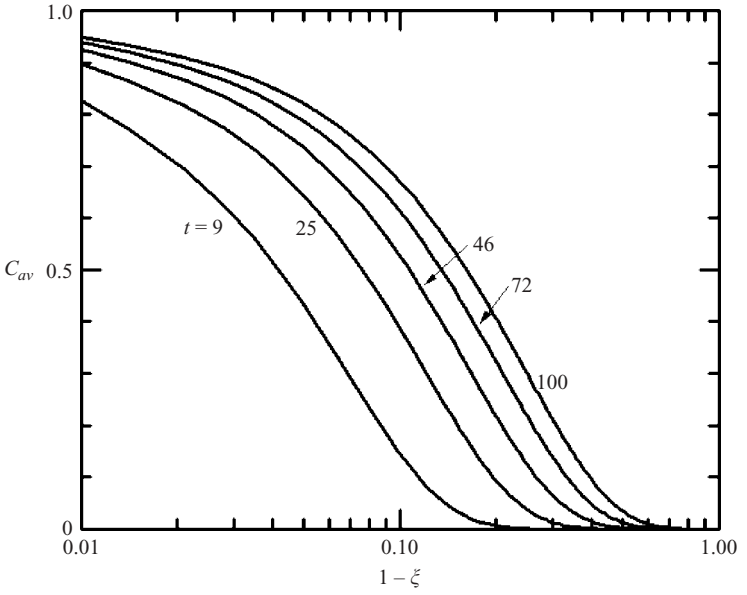


FIGURE 5. Transversal average concentration, $C_{av} = \int_0^1 C\,\mathrm{d}\eta$, within the fluid layer for different values of the dimensionless time. $Pe = 10$; $\phi = 45°$. The contaminative surface extends from $\xi = 0.95$ to $\xi = 1$, where layers connect with each other.

The way the tracer travels through the fluid layer with time is presented in figure 5. It shows the transversal average concentration, $C_{av} = \int_0^1 C\,\mathrm{d}\eta$, within the fluid layer for different values of dimensionless time. With time, the tracer travels farther and the concentration near the upper corner (where $1-\xi \to 0$) increases. The tracer is transported along the slot, but the species accumulates near the corner. This increment in C_{av} implies that $\partial C/\partial\eta$ decreases near the place where the tracer enters, so that the tracer flux through the contaminative surface diminishes with time. Additionally, the tracer transport along the slot is more effective at the beginning of the contaminant process and diminishes with time as a result of the gradual tracer accumulation near the corner.

5.2.3. *Effect of convection on the tracer transport*

The ratio between convective and diffusive transport of the species is given by the Péclet number, and the effect of such a parameter on the tracer transport is presented in figure 6. Five different conditions of Péclet number, including the case of pure diffusion ($Pe = 0$), are shown in figure 6(a). All of them correspond to $\phi = \pi/4$ and the same dimensionless time, $t = 100$, after the tracer transport began near the upper corner. The convective flow enhances the contaminant transport along the slot, and according to (3.8) it must occur whenever the product ΓPe increases. Despite of this improved transport the amassed tracer near the corner increases slightly with Pe. The rate at which the tracer enters the system is given by the Sherwood number on the contaminative surface, $Sh = h_D d/D$, where h_D is the species convective coefficient, d is the layer width and D is the tracer diffusion coefficient in the fluid. The Sherwood number was computed from the numerical results considering that: $Sh = \int_{0.95}^1 [-\partial C/\partial y]\,\mathrm{d}\xi/(1-0.95)$. The Sherwood number diminishes with time, which is shown in figure 6(b), where the effect of the Péclet number on the Sherwood number is presented. As mentioned, before, C_{av} increases near the corner as time goes by, hence the tracer flux through the contaminative surface diminishes with time as

https://doi.org/10.1017/S0022112006002217 Published online by Cambridge University Press

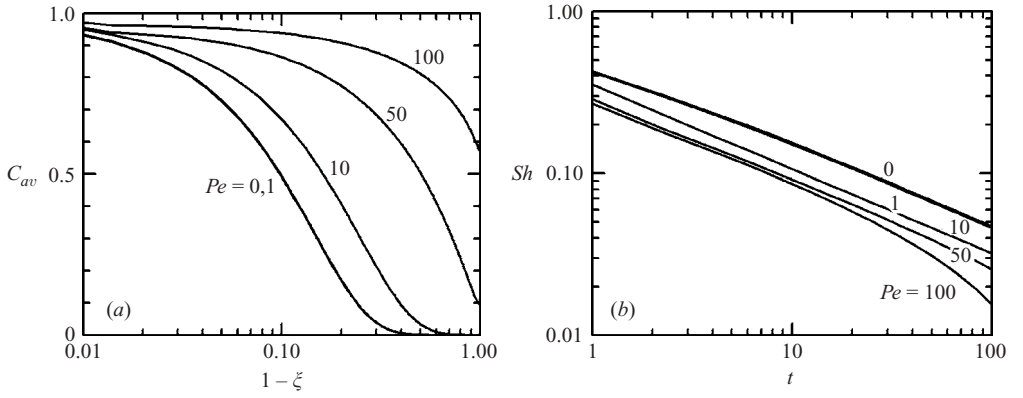


FIGURE 6. (*a*) Effect of the Péclet number on the tracer transport in the fluid layer. The case of pure diffusion ($Pe = 0$) is included $t = 100$; $\phi = 45°$. (*b*) Effect of the Péclet number on the Sherwood number at the contaminative surface with time $\phi = 45°$.

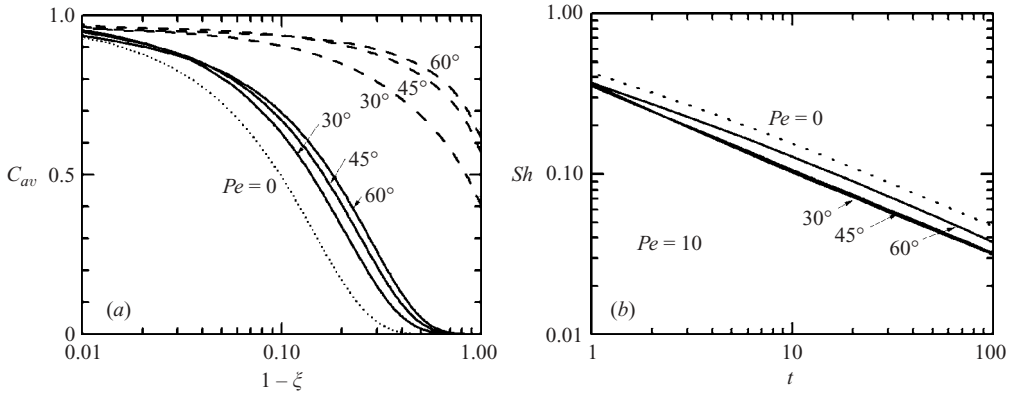


FIGURE 7. Effect of the angle of tilt on the tracer transport. (*a*) Transversal average concentration in the fluid layer for different values of ϕ after a dimensionless time $t = 100$. —, $Pe = 10$; - - -, 100. (*b*) Effect of the angle of tilt on the Sherwood number at the contaminative surface with time.

a result of that gradual tracer accumulation. Also the increment of Péclet number leads to the decrement in *Sh* owing to the particular location of the contaminative surfaces. Although the convective motion is relatively fast near the upper corner, there is a stagnant region where layers connect with each other, near the place where the contaminative surfaces are located. If they were located where the convection effect is important, the Sherwood number would rise with the increment of *Pe*.

5.2.4. *Effect of the angle of tilt on the tracer transport*

Since the tilting angle ϕ affects the temperature distribution in the rock, this angle itself has an important effect on the transport phenomena within the layer. Figure 7(*a*) shows the transversal average concentration in the fluid layer for different values of ϕ, when the dimensionless time is $t = 100$. Cases of pure diffusion ($Pe = 0$), small ($Pe = 10$) and large ($Pe = 100$) Péclet numbers are shown. The tracer transport through the layer is enhanced with the increment of the angle of tilt, since the convective motion becomes more intense as the angle of tilt increases. This effect is more evident

https://doi.org/10.1017/S0022112006002217 Published online by Cambridge University Press

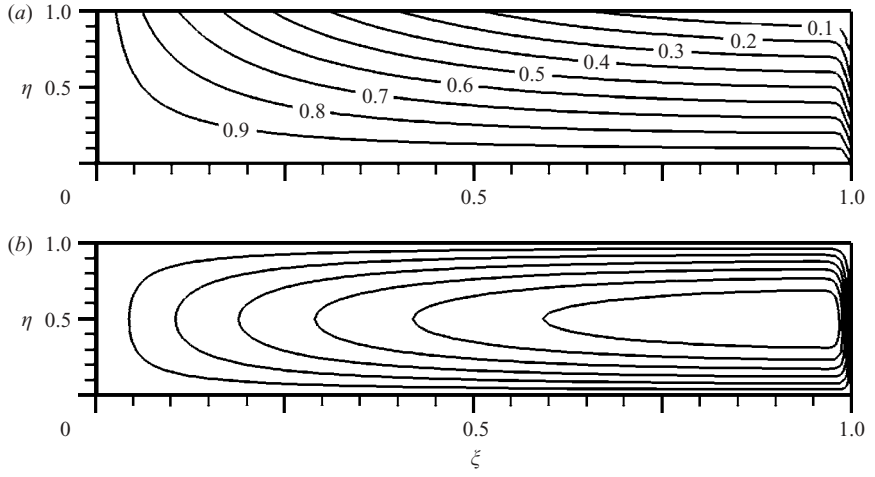


FIGURE 8. (*a*) Dimensionless temperature distribution within the saturated porous layer. (*b*) Streamlines within the porous layer. In this case, $Ra = 1 \times 10^{-5}$, $\Gamma = 0.01$, $\phi = \pi/4$, $\kappa \ll \Gamma$.

at large Péclet numbers. The rate at which the tracer enters the system through the contaminative surface is also affected by the angle of tilt (see figure 7*b*). The Sherwood number diminishes with time and the angle of tilt affects both cases, weak convection ($Pe = 10$) and dominant convection ($Pe = 100$, not shown) in a similar way. The decrement of the Sherwood number with time also depends on the angle of tilt since the accumulated tracer near the contaminative surface changes with ϕ (figure 7*a*), and the least tracer accumulation at $1 - \xi \to 0$ corresponds to $\phi = 60°$.

5.3. *The saturated porous layer*

5.3.1. *The convective flow*

Figure 8(*a*) shows the temperature distribution within the saturated porous layer in the non-orthogonal coordinate system. Again diffusion is the main mean for the heat transfer as a result of the small Rayleigh number, $Ra = 10^{-5}$. Figures 8(*a*) and 3(*a*) look similar because both cases are under the small-Rayleigh-number regime, it means that the resulting weak convective flows just slightly affect the isotherms. Computed streamlines in the non-orthogonal coordinate system are presented in figure 8(*b*). The flow arises longitudinally near the lower wall (where $\theta = 1$) throughout the layer and descends near the upper wall. Close to the upper corner, the flow suddenly changes its direction while at the lower region the change in direction is very slow and gentle. Longitudinal dimensionless velocity profiles in the saturated porous layer are shown in figure 9(*a*). The linear velocity profiles are symmetrical with respect to the middle plane $\eta = 0.5$, and the flow is faster at the upper region. The transversal velocity profile at the middle plane, $\eta = 0.5$ is presented in figure 9(*b*), where it is shown how fast the flow changes its direction at the upper corner and how slow this movement is at the lower region. In the finite layer here analysed, the transversal velocity has an important effect on the shape of the convection cell. The intensity of the convection motion changes along the slot, then it is expected that the transport phenomena take place under different conditions which depend on the location within the finite fracture. From the convective flow of figure 8(*b*) it is clear that the transport phenomena in the transversal direction are mainly by diffusion in $0.7 < \xi < 0.95$, both convection and diffusion are important in $0 < \xi < 0.7$, while convection transport is

https://doi.org/10.1017/S0022112006002217 Published online by Cambridge University Press

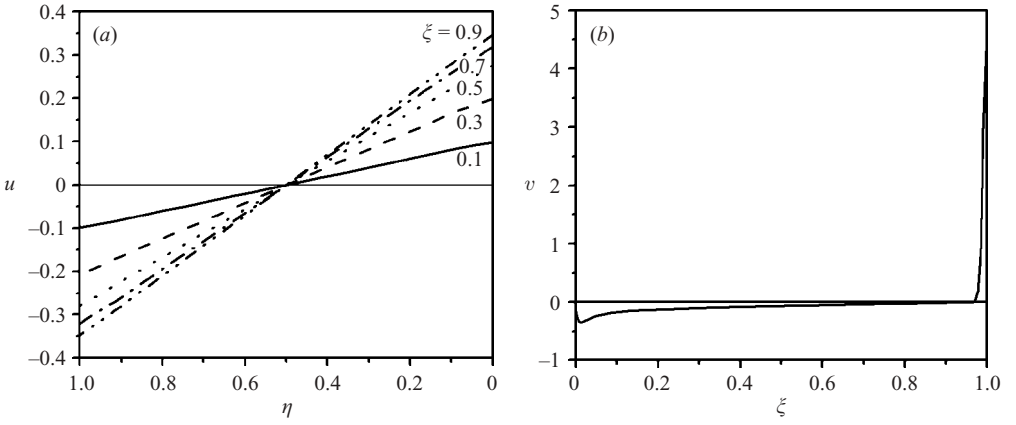


FIGURE 9. (*a*) Longitudinal velocity profiles at different locations within the saturated porous layer. (*b*) Transversal velocity profile at the middle plane, $\eta = 0.5$. In this case, $Ra = 1 \times 10^{-5}$, $\Gamma = 0.01$, $\phi = \pi/4$, $\kappa \ll \Gamma$.

dominant near the upper corner except at the stagnant region located where layers connect with each other. These particular circumstances do not occur within an infinite layer because for such a condition the fluid flow is one-dimensional. Our finite porous layer is under the conduction regime, consequently, the shape of the convective patterns and the dimensionless velocity are not affected by the Rayleigh number. So, figures 8 and 9 are valid for the whole range studied here, $10^{-7} \leqslant Ra \leqslant 10^{-3}$, when $\Gamma = 0.01$ and $\phi = \pi/4$. Again, the effect of the Rayleigh number on the actual velocity is considered in the definition of the dimensionless velocity itself. Moreover, since the angle of tilt affects the shape of the convection cell, this angle also influences the transversal transport phenomena.

5.3.2. *Transient transport of a passive tracer*

The tracer transport in the saturated porous layer has two parameters, to consider. The diffusive Péclet number, Pe, which expresses the convection to diffusion ratio, and the dispersive Péclet number, Pe_α, which represents the dispersive effect itself, the effect obtained by combining convective and diffusive transports in porous media at the pore scale. Suitable values for the dispersive Péclet number are not easily estimated owing to the scarcity of dispersivity coefficients data. Lake (1989) presents a compilation of experimental dispersivity coefficients; however, there are serious discrepancies between measurements corresponding to the same material since these data depend on the characteristic size of the sample. Laboratory measurements where the sample sizes are of the order of 1 m show dispersivity data of the order of 10^{-3} m. In this work it is assumed that $Pe_\alpha \gtrsim 1$, this means that the dispersivity, which is the typical homogeneity length of the porous structure, is equal to or lower than the characteristic length d. The hydrodynamic dispersion is the result of the Taylor dispersion due to macroscopic fluctuations of the velocity on the length scales where the porous structure must be considered inhomogeneous, and it can be neglected when the characteristic Péclet number of the porous medium, $Pe_{hom} = Vl/(D\Phi)$ is small (Linz & Woods 1992). Here V is the maximum velocity of the flow and l is a typical homogeneity length of the porous structure. In the present case $Pe_{hom} = Pe/(\Phi Pe_\alpha)$, thus in our particular conditions the hydrodynamic dispersion can be neglected if $Pe/(\Phi Pe_\alpha) \ll 1$, which also agrees with the information given by (3.9).

https://doi.org/10.1017/S0022112006002217 Published online by Cambridge University Press

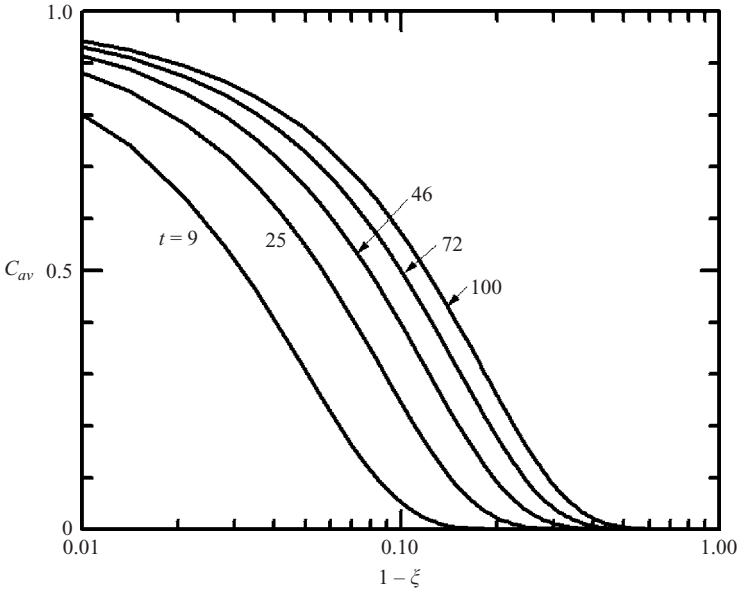


FIGURE 10. Transversal average concentration, $C_{av} = \int_0^1 C\,\mathrm{d}\eta$, within the porous layer for different values of the dimensionless time. The contaminative surface extends from $\xi = 0.95$ to $\xi = 1$, where layers connect with each other. $Pe = 1$; $Pe_\alpha = 10$; $\phi = 45°$.

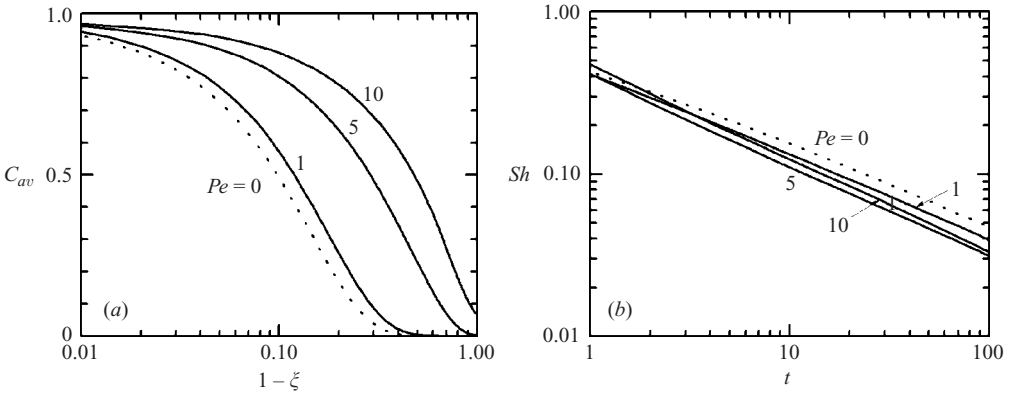


FIGURE 11. (*a*) Effect of the Péclet number on the tracer transport in the porous layer. The case of pure diffusion ($Pe = 0$) is included. $t = 100$. (*b*) Effect of the Péclet number on the Sherwood number at the contaminative surface with time $\phi = 45°$; $Pe_\alpha = 10$.

The way the tracer travels through the porous layer as time goes by is presented in figure 10. It shows the transversal average concentration, $C_{av} = \int_0^1 C\,\mathrm{d}\eta$, within the porous layer for different values of dimensionless time. With time the tracer travels farther, but the concentration near the upper corner (where $1 - \xi \to 0$) increases. Again, this increment in C_{av} near the place where the tracer enters causes decrement of the tracer flux with time. Therefore, the tracer transport along the slot is more effective at the beginning of the contaminant process and diminishes with time.

5.3.3. *Effect of convection on the tracer transport*

The effect of the Péclet number on the tracer transport is presented in figure 11. Four different conditions, including the case of pure diffusion ($Pe = 0$), are shown

https://doi.org/10.1017/S0022112006002217 Published online by Cambridge University Press

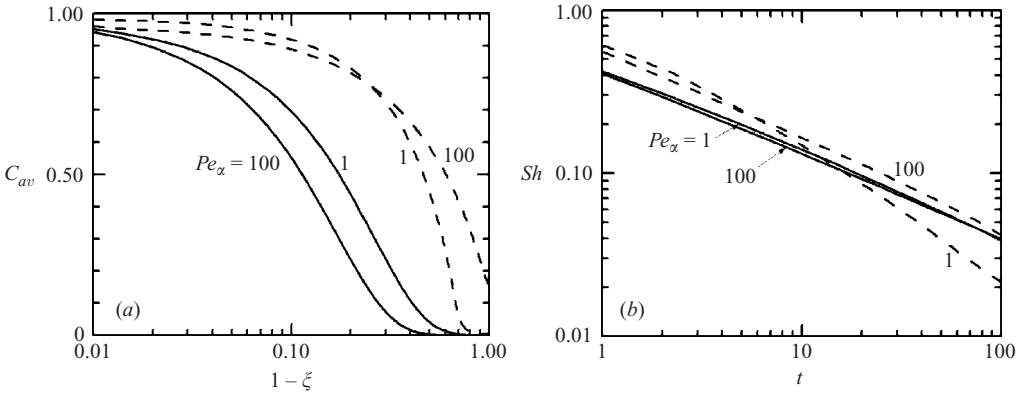


FIGURE 12. Effect of the dispersive Péclet number, Pe_α, on the tracer transport. Solid ($Pe = 1$) and dashed ($Pe = 10$) lines correspond to small and large convective effects, respectively. (a) Transversal average concentration in the porous layer after a dimensionless time $t = 100$. (b) Sherwood number at the contaminative surface with time $\phi = 45°$.

in figure 11(a). All curves correspond to $\phi = \pi/4$ and the same dimensionless time, $t = 100$. It is remarkable the tracer transport enhancement along the slot because of the convective flow; according to (3.9), the convection transport improves when $\Gamma Pe/\Phi$ increases. Additionally, with the increment of the convection effect, the accumulated tracer near the corner also rises. Thus, the Sherwood number diminishes with time; figure 11(b), shows effect of the Péclet number on the Sherwood number. The increment of Pe leads to the decrement in Sh once again, because of the particular location of the contaminative surfaces; they are within the stagnant region where layers connect with each other. Furthermore, the tracer flux through the contaminative surface diminishes with time due to the gradual tracer accumulation near the upper corner.

5.3.4. *Effect of dispersion on the tracer transport*

Figure 12(a) shows the effect of the dispersive Péclet number on the tracer transport. Solid and dashed lines correspond to small ($Pe = 1$) and large ($Pe = 10$) convective effects, respectively. For small convective effects, the increment of dispersive Péclet number diminishes the tracer transport along the layer. This seems to be a condition for which the convection contribution is blocked by the dispersive transport. Indeed, while the passive tracer is taken down by convection, some of this substance diffuses towards the ascending stream because of the high dispersivity, which finally results in a blocking mechanism by dispersion. On the other hand, when the transport is mainly due to convection, $Pe = 10$, the increment of the dispersive Péclet number enhances the tracer transport. Hence, hydrodynamic dispersion does not necessarily improve the tracer transport through the slot its influence depends on the convection conditions. Furthermore, for small and large convection effects the tracer average concentration near the contaminative zone is larger at low Pe_α, which means that dispersion diminishes the tracer accumulation therein.

Then the dispersive effect is also important for the rate the tracer enters into the system (figure 12b). Again, solid and dashed lines correspond to small and large convective effects, respectively. When convection is weak the dispersive effect on the Sherwood number is small, but for dominant convection, the dispersive Péclet number affect the rate the tracer enters the system indeed. At the beginning of the contaminant process the tracer flux through the contaminative surface is larger at

https://doi.org/10.1017/S0022112006002217 Published online by Cambridge University Press

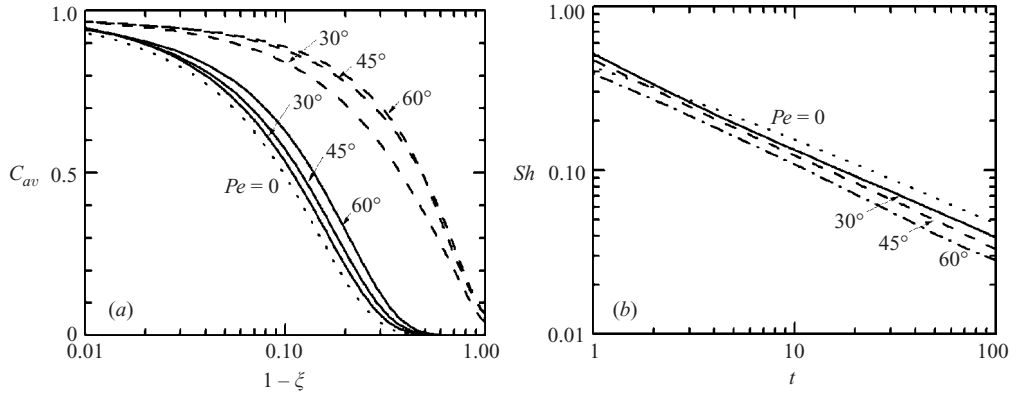


FIGURE 13. Effect of the angle of tilt on the tracer transport in the porous layer. (*a*) Transversal average concentration for different values of ϕ, at a dimensionless time $t = 100$. $Pe_\alpha = 10$; —, $Pe = 1$; - - -, 10. (*b*) Sherwood number on the contaminative surface as time goes by. $Pe = 10$; $Pe_\alpha = 10$.

low Pe_α, and diminishes with time due to the gradual tracer accumulation near the corner. Then, for large times, the increment of the dispersive effect causes a smaller decrement in Sherwood number with time.

5.3.5. *Effect of the angle of tilt on the tracer transport*

Figure 13(*a*) presents the transversal average concentration along the slot for different values of ϕ, at a dimensionless time $t = 100$. The cases of pure diffusion ($Pe = 0$), small ($Pe = 1$) and large ($Pe = 10$) Péclet numbers are shown. The tracer concentration in the layer rises with the increment of the angle of tilt since the convective motion becomes more intense as ϕ increases. This effect is more evident at large Péclet numbers. The rate the tracer enters the system through the contaminative surface diminishes with time, and such rate is only slightly affected by the angle of tilt when convection is weak (not shown), however, for dominant convection the effect of ϕ is considerable, see (figure 13*b*).

6. Conclusions

The steady-state thermal convection and the passive tracer transport within symmetrically interconnected tilted layers, also assumed to be a folded finite layer in a rock slab, have been presented. Two cases were studied, the fluid-filled layer and the isotropic saturated porous layer, both embedded in an impervious rock affected by a vertical temperature gradient. The present study considers the case of a high contrast between the thermal conductivities of rock and layers. The thermal distribution in the rock near the layers is greatly affected because of the sudden change in the thermal conductivity occurring there. The temperature difference between opposite points along the contact surfaces varies with the longitudinal direction. This particular situation is substantially different from that one which appears in the generic case of a single infinite tilted layer. In such a case, the temperature difference between opposite points on the contact surfaces remains constant along the slot, whereas in finite layers such temperature differences vary along the slots because of the end effects, and for the present case such a condition is specially remarkable. Also because of the end effects, the angle of tilt ϕ plays an important role in the thermal process within the rock, particularly when ϕ becomes smaller.

https://doi.org/10.1017/S0022112006002217 Published online by Cambridge University Press

The convective flows within our finite layers were computed for the small-Rayleigh-number regime. Based on previous experimental experience (Sánchez-Cruz 2005; Sánchez *et al.* 2005), we assumed there was no mass exchange between the two interconnected layers. The numerical results show the significance of the transversal velocity, whose intensity changes along the slot. These circumstances do not occur within an infinite fracture because for such a condition the fluid flow is one-dimensional, the transversal velocity component appears because of the end effects. Therefore, the transport phenomena through the transversal direction in finite slots are due to diffusion and convection whereas in infinite slots there exists only diffusion. Additionally, the strength of the convection motion in an infinite slot embedded in a solid slab is maximum when $\phi = \pi/4$, whereas in the present case the intensity of convection augments when the angle of tilt increases.

The transport of a passive tracer that is initially located where layers connect with each other was studied. Despite the weak convective flow, the motion in the layers serves as an effective way of transporting polluting agents and species. The transport of passive substances is strongly modified by convective flows with respect to the pure diffusive transport. The tracer travels along the slot but the species accumulate near the upper corner because the fluid motion is very slow therein. Thus, the tracer transport along the slot is more effective at the beginning of the contaminant process and diminishes with time due to the gradual tracer accumulation near the corner. The convective flow enhances the contaminant transport when ΓPe increases. In porous layers, the increment of the Péclet number leads to the decrement in Sh owing to the particular location of the contaminative surfaces. The hydrodynamic dispersion does not necessarily improve the tracer transport, its influence depends on the convection conditions, and it can be neglected when $Pe/(\Phi Pe_\alpha) \ll 1$. The tracer concentration in the layer increases with the increment of the angle of tilt, specially at large Péclet numbers, since the convective motion becomes more intense as the tilting angle increases.

For demonstration purposes, let us consider typical values used in geological estimations. Assuming water-filled layers, it would be reasonable to suppose $\beta = 3\times10^{-4}\,\mathrm{K}^{-1}$, $\nu = 10^{-6}\,\mathrm{m^2\,s^{-1}}$, $\alpha_f = 10^{-7}\,\mathrm{m^2\,s^{-1}}$, $d = 3.4\times10^{-3}\,\mathrm{m}$, $\Gamma = 10^{-2}$, $D = 10^{-9}\,\mathrm{m^2\,s^{-1}}$ and $\phi = \pi/4$ (Woods & Linz 1992). The geothermal gradient near the surface of the earth is about $G = \Delta T/H = 2.5\times10^{-2}\,\mathrm{K\,m^{-1}}$, therefore in this particular case $Ra = g\beta G d^4/(\nu\alpha_f\Gamma) = 10$ and $Pe = 10$. Thus, at the steady state, we estimate the maximum longitudinal velocity to be $1.5\times10^{-6}\,\mathrm{m\,s^{-1}}$, and 13.5 days after the contaminative process began the tracer concentration is expected to be 10 % of the saturation concentration at 0.13 m from the contaminant source; under pure diffusive conditions, such a concentration would be located at 0.07 m from the contaminant source within the same time. Moreover, we predict the average species convective coefficient on the contaminative surface to be $h_D = 1\times10^{-7}\,\mathrm{m\,s^{-1}}$ at the beginning of the contaminative process, and 13.5 days after then it must diminish to $h_D = 9\times10^{-9}\,\mathrm{m\,s^{-1}}$. In the case of saturated porous layers, let us assume there is water in an unconsolidated sandstone for which it would be reasonable to consider $\beta = 3\times10^{-4}\,\mathrm{K^{-1}}$, $\nu = 10^{-6}\,\mathrm{m^2\,s^{-1}}$, $\alpha_m = 3.5\times10^{-7}\,\mathrm{m^2\,s^{-1}}$, $K = 10^{-10}\,\mathrm{m^2}$, $d = 2\times10^{-2}\,\mathrm{m}$, $\Gamma = 10^{-2}$, $D = 10^{-9}\,\mathrm{m^2\,s^{-1}}$, $\alpha_D = 2\times10^{-3}\,\mathrm{m}$, $\Phi = 0.25$, $\tau = 2.4$, and $\phi = \pi/4$ (Lake 1989; Linz & Woods 1992), then $Ra = Kg\beta G d^2/(\nu\alpha_m\Gamma) \approx 10^{-3}$, $Pe \approx 1$ and $Pe_\alpha = 10$. At the steady state, the maximum longitudinal velocity is estimated to be 20 cm per year approximately, and 3 years after the contaminative process began the tracer concentration is equal to 10 % of C_{sat} at 0.6 m from the contaminant source; with mere diffusive transport such a concentration would be located at 0.46 m from the contaminative source

https://doi.org/10.1017/S0022112006002217 Published online by Cambridge University Press

within the same time. The average species convective coefficient is estimated to be $h_D = 2 \times 10^{-8}\,\mathrm{m\,s^{-1}}$ at the beginning of the contaminative process, and 3 years after then it must diminish to $h_D = 2 \times 10^{-9}\,\mathrm{m\,s^{-1}}$.

So, we have shown useful results for improving the estimation of transport phenomena within slender layers, which are related to other important geophysical processes, e.g. diagenetic alteration, all of them usually concerning the oil and underground water pollution interested industries. The assumptions here considered restrict the results to cases where the layers are embedded within an ideal impervious matrix. Therefore, additional work regarding the actual interaction between the low-permeability porous matrix and its inner layer, as well as the resulting relevant implications in the geophysical context is currently in progress.

F. A. S. acknowledges support from CONACyT through the scholarship 159041. A. M. acknowledges support from Spain Ministerio de Educación, Cultura y Deporte through a sabbatical fellowship Project SAB2002-0137. The authors wish to thank F. J. Higuera from Universidad Politécnica de Madrid, Spain, for the benefit of several discussions and constructive criticism.

Appendix A. Functions referenced in the main text

Functions A to N in (4.5) are as follows:

$$A = -\frac{Pr}{Ra(1+\varepsilon\eta)^4}\left(\frac{\varepsilon^4\xi^4}{\Gamma^2} + \Gamma^2 + 2\varepsilon^2\xi^2\right), \tag{A 1}$$

$$B = \frac{4Pr\varepsilon\xi}{Ra(1+\varepsilon\eta)^3}\left(\frac{\varepsilon^2\xi^2}{\Gamma^2} + 1\right), \tag{A 2}$$

$$C = -\frac{12Pr\varepsilon^2\xi}{Ra(1+\varepsilon\eta)^4}\left(\frac{\varepsilon^2\xi^2}{\Gamma^2} + 1\right) + \frac{1}{(1+\varepsilon\eta)^3}\left[\left(\frac{\partial\psi^0}{\partial y}\right)(\Gamma^2 + \varepsilon^2\xi^2) + \left(\frac{\partial\psi^0}{\partial x}\right)(\varepsilon\Gamma^2\xi + \varepsilon^3\xi^3)\right], \tag{A 3}$$

$$D = -\frac{12Pr\varepsilon^2}{Ra(1+\varepsilon\eta)^4}\left(\frac{3\varepsilon^2\xi^2}{\Gamma^2} + 1\right) + \frac{1}{(1+\varepsilon\eta)^3}\left[\left(\frac{\partial\psi^0}{\partial y}\right)4\varepsilon^2\xi + \left(\frac{\partial\psi^0}{\partial x}\right)(6\varepsilon^3\xi^2 + 2\varepsilon\Gamma^2)\right], \tag{A 4}$$

$$E = \frac{8Pr\varepsilon}{Ra(1+\varepsilon\eta)^3}\left(\frac{3\varepsilon^2\xi^2}{\Gamma^2} + 1\right) - \frac{1}{(1+\varepsilon\eta)^2}\left[\left(\frac{\partial\psi^0}{\partial y}\right)2\varepsilon\xi + \left(\frac{\partial\psi^0}{\partial x}\right)(\Gamma^2 + 3\varepsilon^2\xi^2)\right], \tag{A 5}$$

$$F = -\frac{2Pr}{Ra(1+\varepsilon\eta)^2}\left(\frac{3\varepsilon^2\xi^2}{\Gamma^2} + 1\right), \tag{A 6}$$

$$G = -\frac{24\varepsilon^4\xi Pr}{Ra\Gamma^2(1+\varepsilon\eta)^4} + \frac{2\varepsilon^2}{(1+\varepsilon\eta)^3}\left[\left(\frac{\partial\psi^0}{\partial y}\right) + 3\varepsilon\xi\left(\frac{\partial\psi^0}{\partial x}\right)\right], \tag{A 7}$$

$$H = \frac{24\varepsilon^3\xi Pr}{Ra\Gamma^2(1+\varepsilon\eta)^3} - \frac{2\varepsilon}{(1+\varepsilon\eta)^2}\left[\left(\frac{\partial\psi^0}{\partial y}\right) + 3\varepsilon\xi\left(\frac{\partial\psi^0}{\partial x}\right)\right], \tag{A 8}$$

$$I = -\frac{12\varepsilon^2\xi Pr}{Ra\Gamma^2(1+\varepsilon\eta)^2} + \frac{1}{1+\varepsilon\eta}\left[\left(\frac{\partial\psi^0}{\partial y}\right) + 3\varepsilon\xi\left(\frac{\partial\psi^0}{\partial x}\right)\right], \tag{A 9}$$

https://doi.org/10.1017/S0022112006002217 Published online by Cambridge University Press

$$J = \frac{4\varepsilon\xi Pr}{Ra\Gamma^2(1+\varepsilon\eta)}, \tag{A 10}$$

$$K = -\left(\frac{\partial\psi^0}{\partial x}\right), \tag{A 11}$$

$$L = -\frac{Pr}{Ra\Gamma^2}, \tag{A 12}$$

$$M = -\frac{Pr}{Ra\Gamma^2(1+\varepsilon\eta)}\left(\frac{\varepsilon\xi\sin(\phi)}{\Gamma} + \cos(\phi)\right), \tag{A 13}$$

$$N = \frac{Pr\sin(\phi)}{Ra\Gamma^3}. \tag{A 14}$$

For the case of the fluid layer, functions R to V in (4.6) are:

$$R = \left(\frac{\partial\psi^0}{\partial y}\right)\frac{1}{1+\varepsilon\eta} + \left(\frac{\partial\psi^0}{\partial x}\right)\frac{\varepsilon\xi}{1+\varepsilon\eta} - \frac{2\varepsilon^2\xi}{Ra\Gamma^2(1+\varepsilon\eta)^2}, \tag{A 15}$$

$$S = -\frac{1}{Ra(1+\varepsilon\eta)^2} - \frac{1}{Ra\Gamma^2}\left(\frac{\varepsilon\xi}{1+\varepsilon\eta}\right)^2, \tag{A 16}$$

$$T = \frac{2\varepsilon\xi}{Ra\Gamma^2(1+\varepsilon\eta)}, \tag{A 17}$$

$$U = -\frac{1}{Ra\Gamma^2}, \tag{A 18}$$

$$V = -\left(\frac{\partial\psi^0}{\partial x}\right) \tag{A 19}$$

$$\text{where } \frac{\partial\psi^0}{\partial x} = \frac{1}{1+\varepsilon\eta}\frac{\partial\psi^0}{\partial\xi}, \text{ and } \frac{\partial\psi^0}{\partial y} = \frac{\partial\psi^0}{\partial\eta} - \frac{\varepsilon\xi}{1+\varepsilon\eta}\frac{\partial\psi^0}{\partial\xi}. \tag{A 20}$$

Functions A to F in (4.9) for the porous layer are:

$$A = \frac{2\varepsilon^2\xi}{(1+\varepsilon\eta)^2}, \tag{A 21}$$

$$B = \left(\frac{\varepsilon\xi}{1+\varepsilon\eta}\right)^2 + \left(\frac{\Gamma}{1+\varepsilon\eta}\right)^2, \tag{A 22}$$

$$C = -\frac{2\varepsilon\xi}{1+\varepsilon\eta}, \tag{A 23}$$

$$D = 1, \tag{A 24}$$

$$E = -\left(\frac{\sin(\phi)\varepsilon\xi}{1+\varepsilon\eta} + \frac{\Gamma\cos(\phi)}{1+\varepsilon\eta}\right), \tag{A 25}$$

$$F = \sin(\phi). \tag{A 26}$$

For the case of saturated porous layer, functions R to V in (4.6) are:

$$R = \left(\frac{\partial\psi^0}{\partial y}\right)\frac{1}{1+\varepsilon\eta} + \left(\frac{\partial\psi^0}{\partial x}\right)\frac{\varepsilon\xi}{1+\varepsilon\eta} - \frac{2\varepsilon^2\xi}{\Gamma Ra(1+\varepsilon\eta)^2}, \tag{A 27}$$

$$S = -\frac{\Gamma}{Ra(1+\varepsilon\eta)^2} - \frac{1}{\Gamma Ra}\left(\frac{\varepsilon\xi}{1+\varepsilon\eta}\right)^2, \tag{A 28}$$

$$T = \frac{2\varepsilon\xi}{\Gamma Ra(1+\varepsilon\eta)}, \tag{A 29}$$

https://doi.org/10.1017/S0022112006002217 Published online by Cambridge University Press

$$U = -\frac{1}{\Gamma Ra}, \tag{A 30}$$

$$V = -\left(\frac{\partial \psi^0}{\partial x}\right). \tag{A 31}$$

Functions R to V in (4.12), for the fluid-filled layer, are:

$$R = \frac{\Gamma Pe}{1+\varepsilon\eta}(u - \varepsilon\xi v) - \frac{2\varepsilon^2\xi}{(1+\varepsilon\eta)^2}, \tag{A 32}$$

$$S = -\left(\frac{\Gamma}{1+\varepsilon\eta}\right)^2 - \left(\frac{\varepsilon\xi}{1+\varepsilon\eta}\right)^2, \tag{A 33}$$

$$T = \frac{2\varepsilon\xi}{1+\varepsilon\eta}, \tag{A 34}$$

$$U = -1, \tag{A 35}$$

$$V = \Gamma Pe v, \tag{A 36}$$

and functions R to V in (4.12), for the saturated porous layer, are:

$$R = \left(\frac{\Gamma Pe}{\Phi}u - \frac{\Gamma^2 Pe}{\Phi Pe_\alpha}\frac{\partial|\boldsymbol{u}|}{\partial x}\right)\frac{1}{1+\varepsilon\eta} - \left(\frac{\Gamma Pe}{\Phi}v - \frac{Pe}{\Phi Pe_\alpha}\frac{\partial|\boldsymbol{u}|}{\partial y}\right)\frac{\varepsilon\xi}{1+\varepsilon\eta} - \left(1 + \frac{Pe|\boldsymbol{u}|}{Pe_\alpha\Phi}\right)\frac{2\varepsilon^2\xi}{(1+\varepsilon\eta)^2}, \tag{A 37}$$

$$S = -\left(1 + \frac{Pe|\boldsymbol{u}|}{\Phi Pe_\alpha}\right)\left[\left(\frac{\Gamma}{1+\varepsilon\eta}\right)^2 + \left(\frac{\varepsilon\xi}{1+\varepsilon\eta}\right)^2\right], \tag{A 38}$$

$$T = \left(1 + \frac{Pe|\boldsymbol{u}|}{\Phi Pe_\alpha}\right)\frac{2\varepsilon\xi}{1+\varepsilon\eta}, \tag{A 39}$$

$$U = -\left(1 + \frac{Pe|\boldsymbol{u}|}{\Phi Pe_\alpha}\right), \tag{A 40}$$

$$V = \left(\frac{\Gamma Pe}{\Phi}v - \frac{Pe}{\Phi Pe_\alpha}\frac{\partial|\boldsymbol{u}|}{\partial y}\right), \tag{A 41}$$

$$\text{where } \frac{\partial|\boldsymbol{u}|}{\partial x} = \frac{1}{1+\varepsilon\eta}\frac{\partial|\boldsymbol{u}|}{\partial\xi}, \text{ and } \frac{\partial|\boldsymbol{u}|}{\partial y} = \frac{\partial|\boldsymbol{u}|}{\partial\eta} - \frac{\varepsilon\xi}{1+\varepsilon\eta}\frac{\partial|\boldsymbol{u}|}{\partial\xi}. \tag{A 42}$$

REFERENCES

Bear, J. 1972 *Dynamics of Fluids in Porous Media*. Elsevier.

Davis, S. H., Rosenblat, S., Wood, J. R. & Hewett, T. A. 1985 Convective fluid flow and diagenetic patterns in domed sheets. *Am. J. Sci.* **285**, 207.

Hewett, T. A. 1986 Porosity and mineral alteration by fluid flow through a temperature field. In *Reservoir Characterization* (ed. L. W. Lake & H. B. Carroll Jr), pp. 83–140. Academic.

Lake, L. W. 1989 *Enhanced Oil Recovery*. Prentice–Hall.

Linz, S. J. & Woods, A. W. 1992 Natural convection, Taylor dispersion, and diagenesis in a tilted porous layer. *Phys. Rev.* A **46**, 4869.

Luna, E. 2003 *Inyección de nitrógeno en un yacimiento petrolífero: Caso Cantarell*. PhD thesis, Universidad Nacional Autónoma de México.

Luna, E., Cordova, J. A., Medina, A. & Higuera, F. J. 2002 Convection in a finite tilted fracture in a rock. *Phys. Lett.* A **300**, 449.

Luna, E., Medina, A., Pérez-Rosales, C. & Trevino, C. 2004 Convection and dispersion in a naturally fractured reservoir. *J. Porous Media* **7**, 303.

https://doi.org/10.1017/S0022112006002217 Published online by Cambridge University Press

Medina, A., Luna, E., Perez-Rosales, C. & Higuera, F. J. 2002 Thermal convection in tilted porous fractures. *J. Phys. (Cond. Matter)* **14**, 2467.

Nield, D. A. & Bejan, A. 1999 *Convection in Porous Media*. Springer.

Phillips, O. M. 1991. *Flow and Reactions in Permeable Rocks*. Cambridge University Press.

Riahi, N. 1983 Nonlinear convection in a porous layer with finite conducting boundaries. *J. Fluid Mech.* **129**, 153.

Sanchez, F., Perez-Rosales, C. & Medina, A. 2005 Natural convection in symmetrically interconnected tilted layers. *J. Phys. Soc. Japan* **74**, 1170.

Sanchez-Cruz, F. A. 2005 Convección en medios porosos con fracturas inclinadas: Interacción con el medio poroso externo. PhD thesis, Universidad Nacional Autónoma de México.

Shaughnessy, E. J. & Van Gilder, J. W. 1995 Low Rayleigh number conjugate convection in straight inclined fractures in rock. *Numer. Heat Transfer* A **28**, 389.

Taylor, G. I. 1953 Dispersion of soluble matter in solvent flowing slowly through a tube. *Proc. R. Soc. Lond.* A **219**, 186.

Wang, M., Kassoy, D. R. & Weidman, P. D. 1987 Onset of convection in a vertical slab of saturated porous media between two impermeable conducting blocks. *Intl J. Heat Mass Transfer* **30**, 1331.

Wood, J. R. & Hewett, T. A. 1982 Fluid convection and mass transfer in porous sandstones – a theoretical model. *Geochem. Cosmochem. Acta* **46**, 1707.

Woods, A. W. & Linz, S. J. 1992 Natural convection and dispersion in a tilted fracture. *J. Fluid Mech.* **241**, 59.

https://doi.org/10.1017/S0022112006002217 Published online by Cambridge University Press